PHILOSOPHICAL TRANSACTIONS OF THE ROYAL SOCIETY A MATHEMATICAL, PHYSICAL & ENGINEERING SCIENCES

Terahertz quantum cascade lasers based on resonant phonon scattering for depopulation

Qing Hu, Benjamin S. Williams, Sushil Kumar, Hans Callebaut and John L. Reno

Phil. Trans. R. Soc. Lond. A 2004 **362**, 233-249
doi: 10.1098/rsta.2003.1314

10.1098/rsta.2003.1314

THE ROYAL SOCIETY

Terahertz quantum cascade lasers based on resonant phonon scattering for depopulation

By Qing Hu[1], Benjamin S. Williams[1], Sushil Kumar[1], Hans Callebaut[1] and John L. Reno[2]

[1]*Department of Electrical Engineering and Computer Science and Research Laboratory of Electronics, Massachusetts Institute of Technology, Cambridge, MA 02139, USA*
[2]*Sandia National Laboratories, Department 1123, MS 0601, Albuquerque, NM 87185-0601, USA*

Published online 17 December 2003

We report our development of terahertz (THz) quantum cascade lasers (QCLs), in which the depopulation of the lower radiative level is achieved through resonant longitudinal optical (LO) phonon scattering. This depopulation mechanism, similar to that implemented in all the QCLs operating at mid-infrared frequencies, is robust at high temperatures and high injection levels. The unique feature of resonant LO-phonon scattering in our THz QCL structures allows a highly selective depopulation of the lower radiative level with a sub-picosecond lifetime, while maintaining a relatively long upper level lifetime (more than 5 ps) that is due to upper-to-ground-state scattering. The first QCL based on this mechanism achieved lasing at 3.4 THz ($\lambda \approx 87\,\mu$m) up to 87 K for pulsed operations, with peak power levels exceeding 10 mW at *ca.* 40 K. Using a novel double-sided metal waveguide for mode confinement, which yields a unity mode confinement factor and therefore a low total cavity loss at THz frequencies, we have also achieved lasing at wavelengths longer than 100 μm.

Keywords: terahertz; intersubband; quantum wells; quantum cascade lasers; longitudinal optical (LO) phonon; metal waveguides

1. Introduction

Terahertz (1–10 THz, or 4–40 meV, or 30–300 μm) frequencies are among the most underdeveloped in the electromagnetic spectrum, even though their potential applications are promising for spectroscopy in chemistry and biology, detection of trace gas for military and security applications, astrophysics, plasma diagnostics and end-point detection in dry etching processes, remote atmospheric sensing and monitoring, imaging, non-invasive inspection of semiconductor wafers, high-bandwidth free-space communications and ultra-high-speed signal processing. This underdevelopment is primarily due to the lack of coherent solid-state THz sources that can provide high radiation intensities (greater than 1 mW) and continuous-wave (CW) operations.

One contribution of 16 to a Discussion Meeting 'The terahertz gap: the generation of far-infrared radiation and its applications'.

This is because the THz frequency range falls between two other frequency ranges in which conventional semiconductor devices have been well developed. One is the microwave and millimetre-wave frequency range, and the other is the near-infrared and optical frequency range. Semiconductor electronic devices that use freely moving electrons (such as transistors, Gunn oscillators, Schottky-diode frequency multipliers, and photomixers) are limited by the transit time and parasitic RC time constants. Consequently, the power level of these classical devices decreases as $1/f^4$, or even faster, as the frequency f increases above 1 THz. In contrast to electronic devices that use freely moving electrons to generate radiation, photonic or quantum electronic devices (such as laser diodes) generate radiation by oscillating bound electrons (which give rise to an oscillating displacement current). Consequently, they are not limited by the transient time and/or the RC time constant. However, for conventional bi-polar laser diodes, they are limited to frequencies that correspond to the semiconductor energy gap, which is higher than 10 THz even for narrow-gap lead-salt materials. Thus, the frequency range below 10 THz is inaccessible for conventional semiconductor diode lasers.

Semiconductor quantum wells are human-made quantum-mechanical systems in which the energy levels can be designed and engineered to be any value. Consequently, unipolar lasers based on intersubband transitions (electrons that make lasing transitions between subband levels within the conduction band) were proposed for long-wavelength sources as early as the 1970s (Kazarinov & Suris 1971). However, because of the great challenge in epitaxial material growth and the unfavourable fast non-radiative relaxation rate, it took more than two decades to realize this proposal experimentally. Electrically pumped unipolar intersubband-transition lasers (also-called quantum cascade lasers (QCLs)) at *ca.* 4 μm wavelength were first developed at Bell Laboratories in 1994 (Faist *et al*. 1994). Since then, impressive improvements in performance have been made in terms of power levels, operating temperatures and frequency characteristics at mid-infrared frequencies.

In contrast to the remarkable development of mid-infrared QCLs, the development of THz QCLs below the *reststrahlen* band (*ca.* 8–9 THz in GaAs) turned out to be much more difficult than initially expected (Helm *et al*. 1989), because of two unique challenges at THz frequencies. First, the energy-level separations that correspond to THz frequencies are quite narrow (*ca.* 10 meV). Thus, the selective depopulation mechanism based on energy-sensitive LO-phonon scattering, which has been successfully implemented in mid-infrared QCLs, is not applicable. Second, mode confinement, which is essential for any laser oscillation, is difficult to achieve at THz frequencies. Conventional dielectric-waveguide confinement is not applicable because the evanescent field penetration, which is proportional to the wavelength and is of the order of several tens of micrometres, is much greater than the active gain medium of several micrometres.

In October 2001, almost eight years after the initial development of QCLs, the first QCL operating at 4.4 THz, below the *reststrahlen* band, was developed (Köhler *et al*. 2002). This laser was based on a chirped superlattice structure that had been successfully developed at mid-infrared frequencies (Tredicucci *et al*. 1998). Mode confinement in this THz QCL was achieved using a double-surface plasmon waveguide grown on a semi-insulating (SI) GaAs substrate. Shortly after this breakthrough, a very similar laser structure was developed at 4.6 THz (Rochat *et al*. 2002). Recently, a THz QCL based on bound-to-continuum intersubband transition was developed at

ca. 3.4 THz, which achieved pulse operation at up to 90 K, above 77 K (Scalari *et al.* 2003).

Our group has pursued a different approach to achieve lasing at THz frequencies. We have investigated possibilities of using fast LO-phonon scattering to depopulate the lower radiative level (Xu *et al.* 1997; Williams *et al.* 1999), and using double-sided metal waveguides for THz mode confinement (Xu 1998). After an extensive investigation, these efforts finally bore fruit. In November 2002, a 3.4 THz QCL was developed in which the depopulation of the lower radiative level was achieved through resonant LO-phonon scattering (Williams *et al.* 2003). The performance of this laser device is promising, especially its operating temperatures. One of the laser devices was operated in pulsed mode up to 87 K, producing more than 10 mW of peak power at *ca.* 40 K heat sink temperature (Williams *et al.* 2004*a*). Incorporated with the double-sided metal waveguides, a QCL based on a similar quantum-well structure was developed at *ca.* 102 μm wavelength. It also operated above 77 K (Williams *et al.* 2004*b*). In a parallel effort, we have analysed the transport properties of our THz QCL structures using Monte Carlo simulations (Callebaut *et al.* 2003). In this analysis, we have identified leakage current channels that should be minimized in order to reduce the lasing threshold current densities and to improve the lasing performance at high duty cycles. We summarize key results of these investigations in the following sections.

2. THz gain medium based on resonant LO-phonon scattering for depopulation

Unipolar intersubband lasers are known to yield a high value of gain, because of a large joint density of states as a result of the two subbands tracking each other in k-space; thus electrons emit photons at the same energy regardless of their initial momentum. Consequently, the peak gain is related to the inverted population density Δn in a simple linear fashion:

$$g_{\mathrm{peak}} = \frac{\Delta n}{t}\frac{e^2\omega}{\pi\hbar\varepsilon_{\mathrm{r}}^{1/2}\varepsilon_0 c_0}\frac{z_{ij}^2}{\Delta f} = \frac{\Delta n}{t}\frac{e^2}{2\pi\varepsilon_{\mathrm{r}}^{1/2}\varepsilon_0 c_0 m^*}\frac{f_{ij}}{\Delta f}$$
$$\approx 67\left(\frac{\Delta n}{t}/10^{15}\ \mathrm{cm}^{-3}\right)\frac{f_{ij}}{\Delta f/\mathrm{THz}}\ \mathrm{cm}^{-1}. \qquad (2.1)$$

In equation (2.1), t is the thickness of one module, thus $\Delta n/t$ is the three-dimensional inverted population density in the active region. $z_{ij} = \langle i|z|j\rangle$ is the dipole moment and $f_{ij} = (2m^*\omega z_{ij}^2)/\hbar$ is the dimensionless oscillator strength of the $i \to j$ transition. Δf is the FWHM line width of spontaneous emission in units of Hz (but in units of THz in the last numerical part of equation (2.1)). Clearly, from equation (2.1), there are only *three* parameters that determine the peak material gain, Δn, Δf and f_{ij}; all the other parameters are either fundamental constants or material parameters that are not subject to engineering and manipulation. In our structures, the measured spontaneous emission line width of *ca.* 1 THz (*ca.* 4 meV) is largely limited by lifetime broadening $1/\pi\tau \approx 0.64$ THz for $\tau = 0.5$ ps. For a robust laser operation, we would like to keep the lifetime of the lower lasing state as short as possible, thus a line width much narrower than 1 THz is neither feasible nor desirable. Consequently, we need to concentrate on the optimization of two parameters, Δn and f_{ij}.

From the relation $f_{ij} = (2m^*\omega z_{ij}^2)/\hbar$, to the leading degree, the oscillator strength is determined by the spatial overlap of the two subband wavefunctions that gives a good measure of the radiative dipole moment z_{ij}. Thus, in order to achieve a large value of f_{ij}, the radiative transition should be made spatially vertical. The population inversion Δn is mainly determined by the lifetime of the lower radiative state $\tau_{\rm l}$, of the upper radiative state $\tau_{\rm u}$, and the upper-to-lower state scattering time $\tau_{\rm u\to l}$. A large Δn requires a short $\tau_{\rm l}$, and long $\tau_{\rm u}$ and $\tau_{\rm u\to l}$. The last term, $\tau_{\rm u\to l}$, is a trade-off with the oscillator strength f_{ij}, and it is also determined by the electron temperature, the density and the lasing frequency. Its maximization requires detailed analysis for individual structures. The focus of our investigation has been on reducing $\tau_{\rm l}$ and enhancing $\tau_{\rm u}$. In order to reduce $\tau_{\rm l}$, the lower radiative level should be coupled strongly to the ground states, while, in order to increase $\tau_{\rm u}$, the upper radiative state should be isolated as much as possible from the ground states.

The first successful THz QCLs were designed around chirped superlattice structures (Köhler *et al*. 2002; Rochat *et al*. 2002), which are characterized by large oscillator strengths. However, the depopulation of the lower lasing level relies on resonant tunnelling and electron–electron scattering, which could suffer from thermal backfilling because of narrow subband separations within the miniband of a superlattice. The direct use of LO-phonon scattering for depopulation of the lower state offers several distinctive advantages (Williams & Hu 2001). First, when a collector (ground) state is separated from the lower lasing level by at least the LO-phonon energy (36 meV $\equiv$ 9 THz), depopulation can be extremely fast, and it does not depend much on temperature or the electron distribution. Second, the large energy separation provides intrinsic protection against thermal backfilling of the lower radiative state. Both properties are important in allowing higher temperature operation of lasers at longer wavelengths.

While fast scattering out of the lower lasing level is necessary to achieve population inversion, a long upper-state lifetime $\tau_{\rm u}$ is also highly desirable to increase the level of population inversion. Our previous designs addressed this problem by making the optical transition diagonal (i.e. between states in adjacent wells), so as to reduce upper-state overlap with the collector state (Xu *et al*. 1997). However, this resulted in a small oscillator strength, and in a broad emission line width due to interface roughness. A second design featured a vertical radiative transition (Williams *et al*. 1999), which improved the radiative overlap and had a relatively narrow line width (*ca*. 2 meV $\approx$ 0.5 THz), but depopulation was nonselective and slow, due to the thick barrier needed to reduce parasitic scattering from the upper state.

The key element in the present design was to use *resonant LO-phonon scattering* to selectively depopulate the lower radiative level while maintaining a long upper level lifetime, and it resulted in a breakthrough success. Figure 1 shows the conduction band profile and subband wavefunctions under the designed bias of 64 mV per module. Each module contains four quantum wells, shown inside the dashed box, and 175 such modules are connected in series to form the quantum cascade laser. Under this bias, the electrons are injected from the injector level $1'$ to the upper lasing level 5 through resonant tunnelling. The radiative transition between levels 5 and 4 is spatially vertical, yielding a relatively large oscillator strength ($f_{54} \approx 0.96$). The depopulation is highly selective and fast, as only the lower level 4 is at resonance with a level 3 in the adjacent well, where fast LO-phonon scattering ($\tau_4 \approx 0.5$ ps) takes place to empty electrons from levels 3 and 4 to the injector doublet 1 and 2.

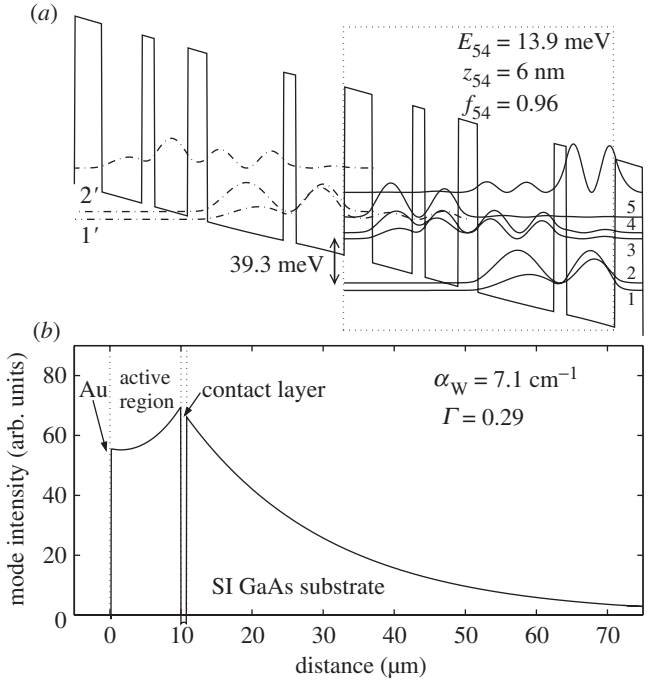

Figure 1. (*a*) Conduction band profile calculated using a self-consistent Schrödinger and Poisson solver (80% conduction band offset) biased at 64 mV per module, which corresponds to a field of 12.2 kV cm^{-1}. The four-well module is outlined. Beginning with the left injection barrier, the layer thickness in angstroms are **54**/78/**24**/64/**38**/148/**24**/94, where bold fonts represent barrier thicknesses. The 148 Å well is doped at 1.9×10^{16} cm^{-3}, yielding a sheet density of 2.8×10^{10} cm^{-2}. (*b*) Optical mode profile of plasmon waveguide.

The scattering time of the upper level 5 to the ground states 2 and 1, due to a relatively thick barrier, is quite long ($\tau_{5\to2,1} \approx 7$ ps), which is important to maintain a population inversion between levels 5 and 4. Electrons in level 1 are then injected to level 5 of the following module (not shown here), completing the cascade pumping scheme.

Molecular beam epitaxy was used to grow 175 cascaded modules, sandwiched between a 60 nm upper contact layer (doped to 5×10^{18} cm^{-3}) and a bottom 800 nm contact layer (doped to 3×10^{18} cm^{-3}) on a semi-insulating (SI) GaAs substrate. Special care was taken to limit the drift in the growth rate to less than 0.7% over the entire growth, to ensure the accuracy of the doping concentration in the active region within 10%, and the Al fraction within 14.5–15.5%. A top non-alloyed ohmic contact was made by evaporating Ti/Au layers on low-temperature-grown GaAs. Wet etching was used to define ridge structures, and NiGe/Au alloyed contacts were made to the lower contact layer at the bottom of the ridge.

Mode confinement in this laser device was achieved using a double-surface plasmon waveguide formed between the top metallic contact and the bottom heavily doped GaAs layer, as in the case of other THz QCLs (Köhler *et al*. 2002; Rochat *et al*. 2002). The calculated mode profile and waveguide loss are shown in figure 1*b*. The calculated waveguide loss of 7.1 cm^{-1} and mode confinement factor $\Gamma \approx 29\%$ are favourable compared with the calculated gain of our laser device. A Fabry–Perot

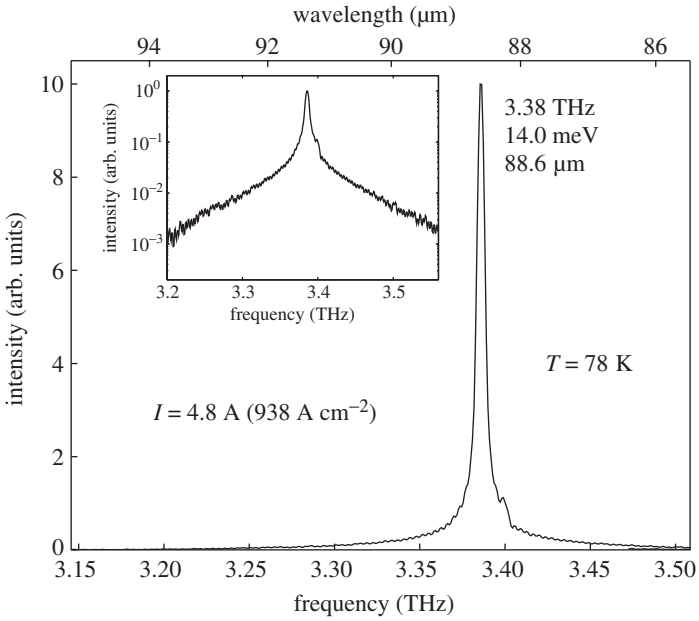

Figure 2. Emission spectrum above threshold biased to 4.8 A at liquid-nitrogen (78 K) heat sink temperature, taken from a laser structure 200 μm wide and 2.6 mm long. The inset shows a semi-log plot of the emission spectrum, which is clearly single mode. The line width is limited by the instrumental resolution of an FTIR (0.125 $cm^{-1} \equiv 3.75$ GHz).

cavity was formed by cleaving the bar structure, and the back facet was coated by evaporating Ti/Au over silicon nitride.

Lasing at 3.38 THz ($\lambda = 88.8\,\mu m$) was obtained in this device at a threshold current density of *ca.* 800 A cm^{-2} at 5 K from a 200 μm wide and 2.6 mm long laser structure. A typical emission spectrum above threshold is shown in figure 2. The emission frequency corresponds to a photon energy of 14.0 meV, close to the calculated value of 13.9 meV. For much of the bias range, the emission is predominantly single mode, although the spectrum shifts toward a higher mode with increasing bias, due to the Stark shift. Pulsed lasing operation is observed up to 87 K with a power level (measured using a thermopile detector, ScienTech Model #360203) of 13 mW at 5 K, and *ca.* 4 mW even at liquid-nitrogen temperature of 78 K, as shown in figure 3*a* (Williams *et al.* 2004*a*). In fact, the spectrum shown in figure 2 was taken with the laser device cooled by liquid nitrogen and using the internal room-temperature pyroelectric detector of a Nicolet FTIR in the fast-scan mode. Measured from a shorter and narrower bar structure (150 μm by 1.18 mm), figure 3*b* displays the voltage versus current, as well as several *P*–*I* curves taken for pulses of increasing width. Even at a high 50% duty cycle, the laser still produces *ca.* 2 mW of peak power, indicating its robustness (Williams *et al.* 2003). It should be pointed out that our present emission power measurement system is far from being optimized. A large fraction of the emitted power is uncollected, especially in the vertical direction where the beam is quite divergent. Thus, the uncorrected power levels cited here are underestimated.

The maximum temperature of pulsed operation of this THz QCL device is encouraging. However, compared with the chirped superlattice and bound-to-continuum THz QCLs, the threshold current density in this laser is quite high (*ca.* 800 A cm^{-2}),

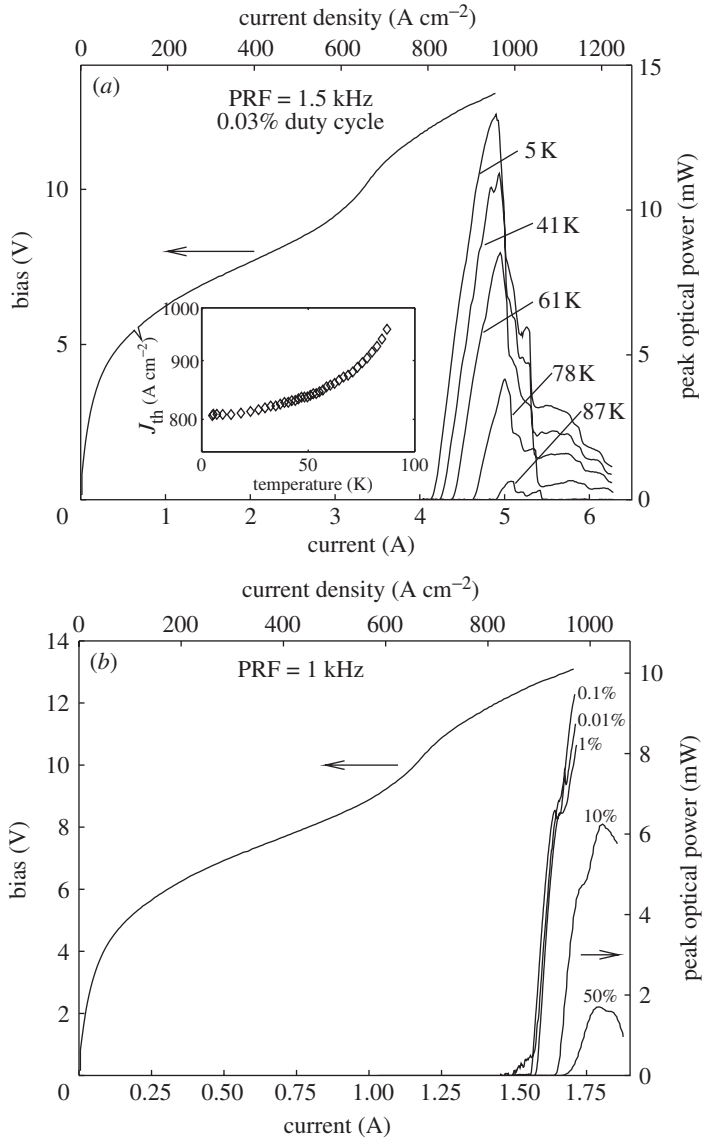

Figure 3. (*a*) *V*–*I* and *P*–*I* at a low duty cycle of 0.03%, taken from the same laser device as in figure 2 at different heat-sink temperatures. (*b*) *V*–*I* and *P*–*I* taken at different duty cycles of a smaller laser structure 150 μm wide and 1.18 mm long. The heat-sink temperatures for the *P*–*I* are 5 K for up to 1% duty cycle, 8 K at 10%, and 15 K at 50%.

which causes a significant heating at high duty cycle operations. The main reason for this high threshold current density is a leakage channel, which we have identified with the aid of Monte Carlo simulations (Callebaut *et al*. 2003). It is clear from figure 1 that, at certain voltage ranges below the designed bias, the injector level 1′ is actually aligned with level 3 that is primarily located in the widest well where fast LO-phonon scattering takes place. Because of this fast scattering, the current density at this bias is quite high, as can be seen with the shoulder structure in the

V–I curve in figure 3 at *ca.* 10 V and *ca.* 600 A cm^{-2}. The device must be biased beyond this point to inject electrons into the upper level 5, and thus with a positive dynamic conductance (which is required for a stable DC bias), the lasing threshold current density will be at least as high as this value. Reduction of this leakage channel and therefore the threshold current density is a main objective of our current investigation. This leakage channel can be reduced by careful designs of the injector and active regions to reduce the coupling between levels 1′ and 3, when these two levels are aligned in energy.

3. THz mode confinement using double-sided metal waveguides

Because of the amphoteric nature of silicon dopants in GaAs, the maximum attainable electron density is *ca.* 5×10^{18} cm^{-3}. At this carrier concentration, the penetration depth is on the order of 1 μm at THz frequencies, causing a significant cavity loss if the lower side of the mode confinement is provided by heavily doped GaAs layers (Rochat *et al.* 2002). The first successful development of THz QCLs used a double surface plasmon layer grown on an SI GaAs substrate for mode confinement. As illustrated in figure 1*b*, the presence of the n$^+$ bottom contact layer enhances the mode intensity in the active region. Although the mode still extends substantially into the substrate, the overlap with heavily doped regions is small, so the free-carrier loss is minimized. This structure is easy to grow and fabricate, and it provides adequate mode confinement for most of the THz QCLs. However, the mode confinement factor Γ in this scheme is far below unity ($\Gamma \sim 0.2$–0.5 for reported lasers). At longer wavelengths ($\lambda > 100$ μm), Γ will become even smaller because of two factors. First, the geometric effect of a longer wavelength reduces the overlap. Second, the dielectric constant $\varepsilon(\omega)$ in the lightly doped active region is reduced by a factor $(1 - \omega_p^2/\omega^2)$ as the frequency ω approaches the plasma frequency $\omega_p = (ne^2/m^*\varepsilon)^{1/2}$. The reduction of $\varepsilon(\omega)$ in the active region compared with that of the SI substrate will further reduce the confinement factor.

Recently, we have developed the first terahertz QCL that uses a double-sided metal waveguide for mode confinement (Williams *et al.* 2004*b*). This metal–semiconductor–metal structure is essentially the same as the micro-strip transmission lines that are widely used for waveguiding at microwave and millimetre-wave frequencies, and the geometry is compatible with the time-modulation (TM) polarization of intersubband transitions. Due to the shallow skin depth in the metal (several hundred angstroms), the waveguide can be made with very low losses and a confinement factor close to unity. In an earlier effort, we developed a process to fabricate such metal waveguide structures using a combination of wafer bonding and selective etching (Xu 1998). THz electroluminescence, but not lasing, was observed in such structures. Mid-infrared QCLs have also been demonstrated using a metal waveguide fabricated via a solder-bonding method. However, at such high frequencies (greater than 12 THz), the loss at the metal surface (scaled as $\omega^{1/2}$) becomes significant so that the metal waveguide QCLs actually performed slightly worse than those using the double-sided surface plasmon waveguides (Unterrainer *et al.* 2002).

The double-sided metal waveguide was fabricated using low temperature In–Au metallic wafer bonding followed by substrate removal. Compared with the Au–Au bonding technique used earlier (Xu 1998), this process yields a much better adhesion and stronger bonding. The schematic of the bonding and substrate removal process

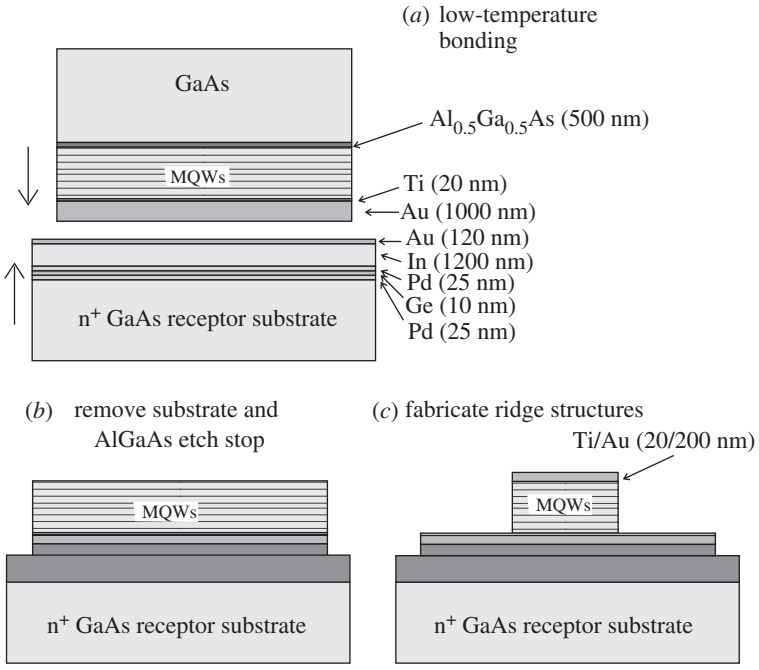

Figure 4. Schematic for the wafer bonding processing for double-sided metal waveguide.

is illustrated in figure 4. Before bonding, the MBE-grown wafer was prepared by evaporating Ti/Au layers (20/1000 nm). An n^+ GaAs receptor substrate was coated with the metal sequence Pd/Ge/Pd/In/Au (25/10/25/1200/120 nm). The purpose of the Pd/Ge/Pd multilayer was to improve the electrical contact to the receptor substrate (Wang *et al*. 1990). Wafer pieces of *ca*. 1 cm^2 were cleaved, aligned, and bonded on a hot plate at 250 °C for *ca*. 10 min while pressure was applied to the stack. Bonding takes place above the melting point of In (157 °C) as the indium wets the surface to fill in any crevices, and then diffuses into the gold layer to reactively form a variety of In–Au alloys (Lee *et al*. 1993; Wang *et al*. 2000). By careful choice of layer thicknesses, all the indium is consumed, and the bonding layer remains robust up to the melting points of the In–Au alloys (*ca*. 450 °C).

The THz QCL structure was grown on an SI GaAs substrate, with a bottom n^+ contact layer that was optimized for mode confinement using the double surface plasmon method. In this way, a direct comparison between the performance of the two mode confinement schemes can be made using the same THz QCL gain medium grown on the same wafer. The one-dimensional mode patterns for the two waveguide structures were calculated using a Drude model solver and are shown in figure 5. Drude scattering times of $\tau = 0.1$ ps and 0.5 ps were used for the heavily doped and lightly doped semiconductor regions, respectively, and $\tau = 0.05$ ps was used for gold. The SI-surface-plasmon waveguide was calculated to have a waveguide loss $\alpha_W \approx 2.04\ cm^{-1}$ and a confinement factor of $\Gamma \approx 0.128$. The $Al_{0.5}Ga_{0.5}As$ layer, which is not normally present in SI-surface-plasmon waveguides, causes a slight reduction in both confinement and loss. The metal waveguide was calculated to have $\alpha_W \approx 17.8\ cm^{-1}$ and $\Gamma \approx 0.98$. Only *ca*. 6 cm^{-1} of that loss is due to the metal and contact layers and the remainder is due to free carrier absorption in the active region. Even

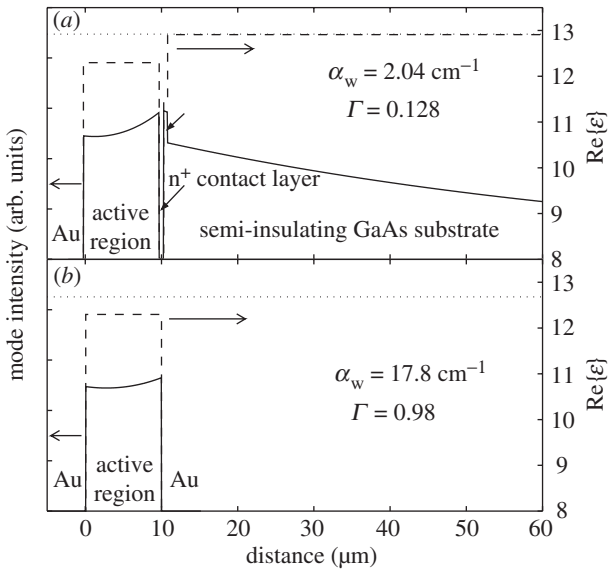

Figure 5. Mode intensities (solid lines) and the real part of the dielectric constant $\varepsilon(\omega)$ (dashed lines) for the (*a*) semi-insulating-surface-plasmon waveguide and (*b*) double-sided metal waveguide. The dotted lines represent the square of the modal effective index.

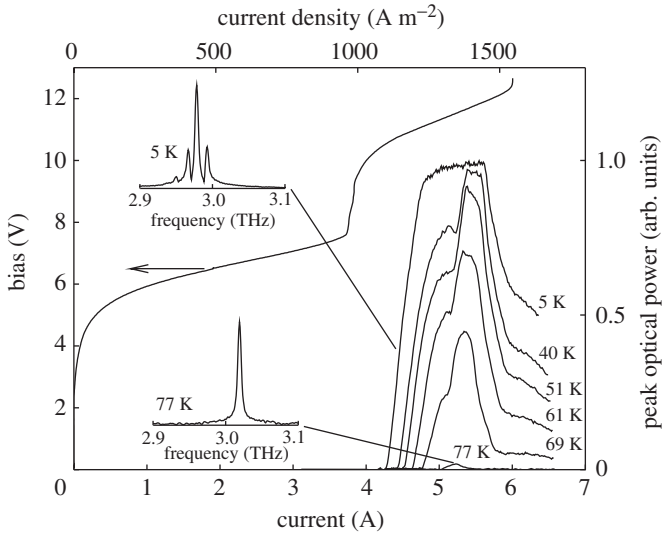

Figure 6. Applied bias versus current at 5 K and emitted light versus current at various temperatures, measured using 100 ns pulses repeated at 1 kHz. Spectra taken at 5 K and 77 K (with liquid-nitrogen cooling) using 100 ns pulses repeated at 10 kHz (10^{-3} duty cycle) are shown.

though α_W/Γ is slightly lower for the SI-surface-plasmon waveguide (*ca.* 16 cm^{-1} compared with *ca.* 18 cm^{-1} for the metal waveguide), the total cavity loss $(\alpha_W + \alpha_m)/\Gamma$ (α_m is the mirror loss) is noticeably higher for a high reflectivity (HR) facet coated cavity length of *ca.* 2 mm (*ca.* 37 cm^{-1} compared with *ca.* 20 cm^{-1} for the metal waveguide structure).

The gain medium quantum-well structure is similar to that shown in figure 1, except there are three injector wells and the emission frequency is designed for a lower value. Lasing was observed in a 150 μm wide, 2.59 mm long metal waveguide device in pulsed mode up to a heat sink temperature of 77 K. Light versus current characteristics and spectra for this device are shown in figure 6. At 5 K, emission takes place from 2.94 THz ($\lambda = 102\,\mu$m) to 3.06 THz ($\lambda = 98\,\mu$m) as the bias is increased. At 77 K, emission is single mode at 3.02 THz, and the spectrum was taken with the laser cooled by liquid nitrogen. The threshold current density is high, $J_{\rm th} \approx 1100\,{\rm A\,cm^{-2}}$ at 5 K, for the same reason as the 3.4 THz laser but is worse at lower frequencies. Because of this high threshold current density and associated heating, the maximum duty cycle is limited, as lasing occurs only over the first 2 μs of an applied pulse.

Nonetheless, the observation of terahertz lasing using a metal waveguide confirms its effectiveness for long wavelength operations. In comparison, devices of similar dimensions (150 μm wide and 2.7 mm long, HR facet coated) that were fabricated using the SI-surface-plasmon waveguide failed to lase at any temperature. This direct comparison unambiguously showed the clear advantage of metal waveguides for THz mode confinement. This scheme will become increasingly advantageous for longer wavelengths, whereas the confinement factor Γ for the SI-surface-plasmon waveguides decreases even further. The reduction of Γ is due both to a geometric effect as the wavelength grows relative to the active region thickness and to the $(1-\omega_{\rm p}^2/\omega^2)$ reduction of the dielectric constant in the active region. As a result of this reduction by the free carriers, the mode extends further into the substrate, where the dielectric constant is higher (figure 5*a*), or even becomes unbound below some cut-off frequency (2.8 THz at our doping level in the active region). The reduction in Γ may be mitigated by increasing the thickness of the n^+ contact layer, or by decreasing the active region doping, but this comes at a cost of increased loss or reduced design flexibility. On the other hand, Γ for the double-sided metal waveguide is always close to unity regardless of the doping concentration in the active region. This important advantage will be valuable or even crucial in the effort to extend QCL operation to even longer wavelengths.

4. Analysis of the transport properties of THz QCLs based on Monte Carlo simulations

Despite the similarity between mid-infrared and THz QCLs, there is a qualitative difference in their dynamics of electron transport. For mid-infrared QCLs, the radiative transition energy $\hbar\omega$ exceeds the LO phonon energy $\hbar\omega_{\rm LO}$ and electron transport is dominated by LO-phonon scattering, which is approximately temperature and density independent. As a result, analysis of mid-infrared QCLs is usually based on a conventional rate-equation approach, in which all the rates are assumed to be constant. In the THz frequency range however, where $\hbar\omega < \hbar\omega_{\rm LO}$, only the high-energy tail of a hot-electron distribution is subject to LO-phonon scattering, which results in a significantly higher temperature sensitivity for the electron transport and a far greater importance of electron–electron (e–e) scattering. If a rate-equation approach is used to analyse the transport properties of THz QCLs, then many of the rates are no longer constant and they depend on the injection levels of the device under operation, thus making the rate equations highly nonlinear. The long delay in the

development of THz QCLs is testimony to the difficulty of achieving population inversion involving these complicated transport mechanisms. It is thus important to be able to quantitatively model these transport processes for the design of suitable THz QCLs for operation over broader frequency ranges and at higher temperatures.

Our transport analysis is based on Monte Carlo (MC) simulations, which have been used to analyse and design mid-infrared and THz QCLs (Köhler *et al*. 2002). Compared with conventional rate-equation analysis, the MC method is especially useful for THz QCLs, as it does not rely on a specific assumption for carrier distributions and can easily handle temperature- and density-dependent scattering times. The MC simulation follows a conventional scheme for an ensemble (*ca*. 10^4) of particles, with a focus on e–e and electron-phonon (e–ph) interactions involving the electrons in one module of the device under study. Only interactions with electrons in states belonging to the same or a neighbouring module are considered. An electron that scatters out of a module is re-injected with identical in-plane k-vector into a subband equivalent to its destination subband, in accordance with the spatial periodicity of the QCLs.

Using this numerical simulation tool, we have analysed transport properties of many intersubband THz emitters, including our own devices and other ones published in the literature. Because of the availability of detailed experimental results, here we focus mainly on the 3.4 THz QCL structure shown in figure 1, with the key results summarized in figure 7. We used a 25 K lattice temperature throughout the simulation, which accounts for the temperature rise during a 100 ns pulsed operation with a heat sink temperature of 5 K.

In figure 7*a*, the first increase in current density occurs in a bias range of *ca*. 35–45 mV per module, where the injector level $n = 1'$ becomes aligned with $n = 3$, which is primarily located in the widest well where fast LO-phonon scattering takes place. The narrow anti-crossing gap between these two levels (*ca*. 0.6 meV) indicates that the calculated peak current density of nearly 2000 A cm^{-2} at *ca*. 45 mV per module (not shown) is a severe overestimation, as wavefunction localization due to dephasing in real devices reduces the coupling between $n = 1'$ and $n = 3$. Still, this parasitic channel carries a significant amount of current, as is evident from the experimentally observed current shoulder at *ca*. 45 mV per module. This detailed transport analysis points out the direction to reduce the threshold current density: reduce this parasitic channel significantly. This can be achieved by reducing the coupling between the injector ground state and the upper LO-phonon resonant state by adding more wells to the active or injector regions, or alternatively by increasing the thickness of the barriers between these two states.

At biases exceeding 50 mV per module, the $n = 2'$ and $n = 1'$ doublet injects carriers into the upper radiative level $n = 5$, yielding a gain as shown in figure 7*d*. The injector ground state $n = 1'$ and $n = 5$ line up at the designed bias of 65 mV per module, reaching the maximum available gain of 68 cm^{-1}. In comparison, we achieved lasing from a 1.18 mm long Fabry–Perot ridge with one facet HR coated (facet loss $\alpha_{\mathrm{m}} = \ln(1/R)/2L$), but no lasing with both facets uncoated ($\alpha_{\mathrm{m}} = \ln(1/R)/L$). Hence the peak gain value is bounded by the total cavity losses of these two structures, shown as the two horizontal lines in figure 7*d*. As shown in figure 7*d*, the calculated maximum gain slightly exceeds the upper bound of the range inferred from the measured results.

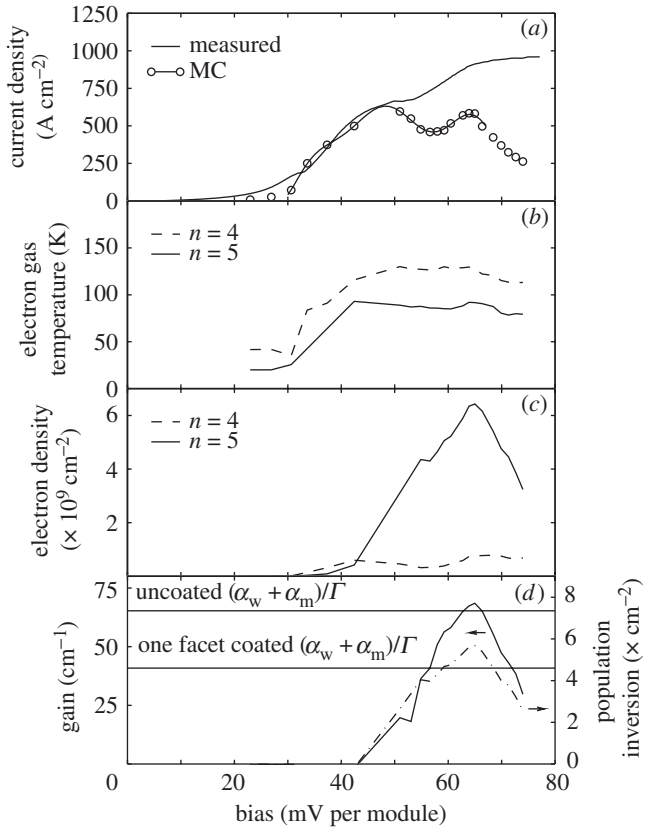

Figure 7. (*a*) Current density for a range of biases. The injection anti-crossing occurs at 65 mV per module. The measured current is represented as a full line. A large parasitic current peak of *ca.* 2000 A cm^{-2} at *ca.* 45 mV per module was omitted from the simulation results. (*b*) Electron temperature T_e for the subbands involved in the radiative transition, $n = 4$ and $n = 5$. (*c*) The population density in $n = 4$ and $n = 5$. (*d*) Material gain for different biases. Also indicated are the calculated threshold gain values for a 1180×150 μm^2 ridge structure, with uncoated facets and with one facet HR coated.

The predicted peak current density of 580 A cm^{-2}, however, falls well short of the measured value of 915 A cm^{-2}. The difference between the measurement and simulation is too large to be accounted for by the absence of a minor transport mechanism, and will be even greater if dephasing scattering and wavefunction localization are considered. The same discrepancy appears to be present in simulated results of other devices where e–e scattering plays an important role in the electron transport. For example, for the three-level structure described in Williams *et al.* (1999), the predicted current density of 110 A cm^{-2} is much lower than the measured *ca.* 300 A cm^{-2}. Also, for the device described in Williams *et al.* (2001), the calculated current density of 55 A cm^{-2} is less than the reported 105 A cm^{-2}. As discussed earlier, for THz QCL structures at low temperatures, e–e scattering plays an important role in the transport processes. The formula that we used in calculating the e–e scattering rates includes a correction from Mosko *et al.* (1995). This correction, which we have verified both analytically and numerically, results in a

factor-of-four lower e–e scattering rate than in Jacoboni & Lugli (1990). Because of this slower e–e scattering rate in our simulations, our analysis of structures similar to that shown in figure 1 has always slightly overestimated the gain and substantially underestimated the current densities.

Even though the slower e–e scattering in our calculations is puzzling, this discrepancy will become much less of an issue or even moot as we focus on the transport properties of THz QCLs at lattice temperatures above 100 K. At such elevated temperatures, thermally activated LO-phonon scattering becomes a dominant process in all the intersubband transitions. A much more serious and challenging problem in our transport analysis is how to deal with wavefunction localization caused by dephasing scattering. In all the published studies on transport properties in QCL structures, the entire multiple quantum-well structure is treated as a coherent quantum mechanical system, for which Schrödinger's equation is solved to yield spatially extended states. Consequently, transport processes are modelled as intersubband scattering among these spatially extended states. In this coherent picture, both the injection to the upper radiative level and removal of electrons from the lower radiative level tend to be quite efficient. As a result, our transport analysis based on this coherent model predicted appreciable levels of gain in most of the structures that we have experimentally investigated for THz lasing. In real devices, dephasing scattering (due to interface roughness, alloy, and impurity scatterings) localize wavefunctions, making transport between weakly coupled states (characterized by a small anti-crossing gap between these states) mostly an incoherent tunnelling process. This incoherent sequential tunnelling process is much less efficient than the injection and removal rates predicted by the coherent model. In our experimental investigations, despite the optimistic predictions from the coherent model, only quantum-well structures similar to that shown in figure 1 have achieved lasing. A possible solution to this problem is to start from a tight-binding model in a density-matrix formalism, where the dephasing scattering comes in naturally in the reduction of the coupling/transport among spatially localized states (Kazarinov & Suris 1971). It is a challenging task to incorporate this model in a Monte Carlo simulation tool, especially for complicated structures that include many quantum wells even in one module. This task is currently under investigation.

We thank S. Goodnick for generously allowing us to adapt his Monte Carlo simulation code. This work is supported by AFOSR, NASA and the NSF. Sandia is a multiprogram laboratory operated by Sandia Corporation, a Lockheed Martin company, for the United States Department of Energy under Contract DE-AC04-94AL85000.

References

Callebaut, H., Kumar, S., Williams, B. S., Hu, Q. & Reno, J. L. 2003 Analysis of transport properties of THz quantum cascade lasers. *Appl. Phys. Lett.* **83**, 207–209.

Faist, J., Capasso, F., Sivco, D. L., Sirtori, C., Hutchinson, A. L. & Cho, A. Y. 1994 Quantum cascade laser. *Science* **264**, 477.

Helm, M., England, P., Colas, E., De Rosa, F. & Allen Jr, S. J. 1989 Intersubband emission from semiconductor superlattices excited by sequential resonant tunneling. *Phys. Rev. Lett.* **63**, 74.

Jacoboni, C. & Lugli, P. 1990 *The Monte Carlo method for semiconductor device simulations.* Springer.

Kazarinov, R. F. & Suris, R. A. 1971 Possibility of the amplification of electromagnetic waves in a semiconductor with a superlattice. *Sov. Phys. Semicond.* **5**, 707–709.

Köhler, R., Tredicucci, A., Beltram, F., Beere, H. E., Linfield, E. H., Davies, A. G., Ritchie, D. A., Iotti, R. C. & Rossi, F. 2002 Terahertz semiconductor–heterostructure laser. *Nature* **417**, 156.

Lee, C. C., Wang, C. Y. & Matijasevic, G. 1993 Au–In bonding below the eutectic temperature. *IEEE Trans. Comp. Hybrids Manufact. Technol.* **16**, 311.

Mosko, M., Moskova, A. & Cambel, V. 1995 Carrier–carrier scattering in photoexcited intrinsic GaAs quantum wells and its effect on femtosecond plasma thermalization. *Phys. Rev.* B **51**, 16 860.

Rochat, M., Ajili, L., Willenberg, H., Faist, J., Beere, H., Davies, G., Linfield, E. & Ritchie, D. 2002 Low-threshold terahertz quantum-cascade lasers. *Appl. Phys. Lett.* **81**, 1381.

Scalari, G., Ajili, L., Faist, J., Beere, H., Linfield, E., Ritchie, D. & Davies, G. 2003 Far-infrared ($\lambda \approx 87\ \mu$m) bound-to-continuum quantum-cascade lasers operating up to 90 K. *Appl. Phys. Lett.* **82**, 3165.

Tredicucci, A., Gmachl, C., Wanke, M. C., Capasso, F., Hutchinson, A. L., Sivco, D. L., Chu, S.-N. G. & Cho, A. Y. 1998 High performance interminiband quantum cascade lasers with graded superlattice. *Appl. Phys. Lett.* **73**, 2101.

Unterrainer, K., Colombelli, R., Gmachl, C., Capasso, F., Hwang, H. Y., Sergent, A. M., Sivco, D. L. & Cho, A. Y. 2002 Quantum cascade lasers with double metal-semiconductor waveguide resonators. *Appl. Phys. Lett.* **80**, 3060.

Wang, L. C., Wang, X. Z., Lau, S. S., Sands, T., Chen, W. K. & Kuech, T. F. 1990 Stable and shallow PdIn ohmic contacts to n-GaAs. *Appl. Phys. Lett.* **56**, 2129.

Wang, T. B., Shen, Z. Z., Ye, R. Q., Xie, X. M., Stubhan, F. & Freytag, J. 2000 Die bonding with Au/In isothermal solidification technique. *J. Electron. Mater.* **29**, 443.

Williams, B. S. & Hu, Q. 2001 Optimized energy separation for phonon scattering in three-level terahertz intersubband lasers. *J. Appl. Phys.* **90**, 5504.

Williams, B. S., Xu, B., Hu, Q. & Melloch, M. R. 1999 Narrow-linewidth terahertz intersubband emission from three-level systems. *Appl. Phys. Lett.* **75**, 2927.

Williams, B. S., Callebaut, H., Hu, Q. & Reno, J. L. 2001 Magnetotunneling spectroscopy of resonant anticrossing in terahertz intersubband emitters. *Appl. Phys. Lett.* **79**, 4444.

Williams, B. S., Callebaut, H., Kumar, S., Hu, Q. & Reno, J. L. 2003 3.4 THz quantum cascade laser based on LO-phonon scattering for depopulation. *Appl. Phys. Lett.* **82**, 1015.

Williams, B. S., Kumar, S., Callebaut, H., Hu, Q. & Reno, J. L. 2004*a* 3.4 THz quantum cascade lasers operating above liquid-nitrogen temperatures. (Submitted.)

Williams, B. S., Kumar, S., Callebaut, H., Hu, Q. & Reno, J. L. 2004*b* Terahertz quantum-cascade laser at $\lambda \approx 100\ \mu$m using metal waveguide for mode confinement. (Submitted.)

Xu, B. 1998 Development of intersubband terahertz lasers using multiple quantum well structures. PhD thesis, Massachussetts Institute of Technology, Cambridge, MA, USA.

Xu, B., Hu, Q. & Melloch, M. R. 1997 Electrically pumped tunable terahertz emitter based on intersubband transition. *Appl. Phys. Lett.* **71**, 440.

Discussion

H. Roskos (*Physikalisches Institut, Johann Wolfgang Goethe-Universität, Frankfurt-am-Main, Germany*). For the amplifier structure, since the external mode is likely to be very different, would it not be quite a challenge to couple into the plasmon waveguides? Would tremendous coupling losses not be expected in this case?

Q. Hu. For the surface plasmon waveguide, there is tremendous mode leakage into the substrate, but the substrate is undoped—so it does not really cause waveguide

losses. In fact, we are doing two-dimensional modelling of the surface plasmon waveguide. There is something new in this—the total waveguide loss and the confinement factor depend on how far the contact pads are placed away from the ridge. For the metal waveguide, which acts like micro-strip transmission lines, it is an irrelevant issue. Also, coupling into a micro-strip transmission line is something that every microwave engineer knows how to do!

J. Faist (*Institute of Physics, University of Neuchâtel, Switzerland*). To make a THz laser operating closer to room temperature, it seems clear that, since the optical phonon is there, you have to take advantage of if it to remove electrons from the lower state. Since you have developed a Monte Carlo simulation, I assume that you have run it at higher temperatures, which is always easier than undertaking measurements on a real device! What is the potential for higher temperature operation?

Q. Hu. I initially thought that an ability to perform Monte Carlo simulations was crucial in order to obtain a working THz laser. After about a year and a half now, I have very strong reservations. There are two issues. The first one is minor: the discrepancy between the measured and calculated currents. Somehow, the modelled electron scattering rate is much slower than would be deduced from experiment, and thus the model slightly overestimates the gain. We still have not solved this problem. But, because when you move to above 100 K the LO phonon scattering dominates, one can live with this. The main problem is the localization issue, in our model and all models I have seen. The models solve the whole structure quantum mechanically as one coherent system. You then have extended states and all the transport models have intersubband scattering processes, which tend to be very fast. From our model, there is a lot of gain in all the structures we have studied, but only two actually lase. How to handle localization, owing to dephasing, is the key issue. We are addressing this now, by implementing a tight binding model in a density matrix formalism, but it is not trivial! I have very strong reservations about how successful simulations of THz lasers are likely to be.

J. Faist. In his Monte Carlo simulations, Professor Fausto Rossi (Köhler *et al*. 2001) (Polytechnic University of Turin, Italy) claimed that you actually need electron–electron scattering in order to obtain a working THz laser. My personal belief is that the upper state lifetime is much more limited by interface roughness than electron–electron scattering. What is the mechanism that you did put in your Monte Carlo simulation?

Q. Hu. If your photons are above 100 K, then LO phonons become more and more dominant, and thus give rise to the limiting-scattering mechanism. At lower temperatures, it really depends on the structure and who has grown it.

H. Roskos. You compared spectroscopy in the mid-infrared and THz frequency ranges. At THz frequencies, you probe higher populated states. What, though is the advantage of doing this, because, for thermal populations in a two-level system, whatever you gain in probing the upper state, you lose with an increased signal-to-noise ratio?

Q. Hu. In the mid-infrared (at room temperature, in the Earth environment), you perform spectroscopy to identify molecules, and there are very few electrons in the upper level. If you try to do emission spectroscopy, the molecules do not emit. You

thus have to undertake measurements *in situ*, passing a laser beam through the gas to a detector. This is not really very versatile. But in the THz range, you have molecules at room temperature in excited states. You thus have molecules at room temperature that will emit. Using THz communication techniques, one can passively mode-lock using a heterodyne receiver, which is something that can be built if one has a local oscillator.

G. Smith (*Department of Physics and Astronomy, University of St Andrews, UK*). Can you say a little more about the advantages of surface plasmons compared with metal waveguides. At what frequency does it become preferable to use one rather than the other?

Q. Hu. Below 10 THz, a metal waveguide is always advantageous. It has pretty much a unity mode confinement factor, with surface losses increasing as the square root of frequency. However, the fabrication is much more involved, and above 5 THz the performance of surface plasmon waveguides is very similar. Thus, if you want a simple fabrication route, you can use surface plasmon waveguides above, say, 4 THz. Below 2 THz, at our doping levels, mode confinement becomes really problematic. At long wavelength, it gets worse for two reasons. First, there is a simple geometric effect. Second, in the active region, the real part of the dielectric constant falls and the mode is actually moved into the substrate. At our doping concentration, and at frequencies of 2.8 THz and below, you get no confinement.

G. Smith. What do you see as the main competition in terms of providing sources? For example, there has been some recent interesting work on optical parametric oscillators in Japan.

Q. Hu. That is a pulsed, not continuous, wave-generation technique. From an electronics background, I always prefer a convenient, compact solid-state source!

Additional reference

Köhler, R., Iotti, R. C., Tredicucci, A. & Rossi, F. 2001 Design and simulation of terahertz quantum cascade lasers. *Appl. Phys. Lett.* **79**, 3920–3922.